

Low loss monolithic barium titanate on insulator integrated photonics with intrinsic quality factor > 1 million

Gwan In Kim^{1,†}, Jieun Yim², and Gaurav Bahl²

¹ Department of Electrical & Computer Engineering,

² Department of Mechanical Science and Engineering,
University of Illinois at Urbana–Champaign, Urbana, IL 61801 USA

† Corresponding author: gikim2@illinois.edu

Abstract

Barium titanate (BTO) has been experiencing a surge of interest for integrated photonics technologies because of its large nonlinear optical coefficients, especially the Pockels coefficient, and in part due to newly available thin-film substrates. In this work, we report on the development of a redeposition-free dry etching technique for monolithic BTO-on-insulator photonics, that produces very low-roughness and high-verticality waveguides. Using this, we experimentally demonstrate the first BTO microresonators with intrinsic Q-factor > 1 million, and waveguide propagation loss as small as 0.32 dB/cm, representing the lowest losses reported in any BTO-based integrated platform to date. We additionally demonstrate Mach-Zehnder amplitude modulators with $V_{\pi}L = 0.54$ V·cm and effective electro-optic coefficient $r_{\text{eff}} = 162$ pm/V.

Barium titanate (BaTiO₃ or BTO) has drawn significant interest for electro-optic (EO) applications due to its exceptionally large Pockels coefficient (bulk measurement $r_{42} = 1640$ pm/V [1]) and there have been several efforts to bring this advantage to integrated photonics. The earliest attempts primarily focused on hybrid integration of BTO thin films with silicon [2–7], silicon nitride [8–11] or silicon dioxide [12] to enable EO functionality without directly patterning the BTO layer. More recently, the emergence of BTO-on-insulator substrates [10, 13] has opened the possibility of full optical confinement entirely within crystalline BTO waveguides. This shift toward monolithic platforms offers new opportunities to fully harness the Pockels coefficient and other nonlinear optical properties of BTO [14–20].

Presently, etching technology for BTO-on-insulator substrates for monolithic integrated photonics remains in an early stage. In particular, superior quality

dry etches that produce smooth and highly vertical sidewalls are still underdeveloped, and yet are essential to minimize scattering and bending losses. Initial attempts for BTO processing have relied on conventional fluorine or chlorine based dry etching chemistries [21, 22]. However, these processes tend to generate non-volatile barium fluoride and chloride byproducts, which adhere to the etched sidewalls resulting in surface roughness and increased optical scattering. These byproducts are difficult to remove without high temperature processing [22], and such methods are not conducive for BTO due to its low Curie temperature. An alternative approach is Ar⁺ ion milling [15, 16], which relies on physical ion bombardment, avoiding chemical byproducts and achieves good sidewall verticality. However, here too it is common to find physical redeposition of sputtered material onto the etched sidewalls, which results in degraded surface quality. While similar redeposition occurs during Ar⁺ etching of LiNbO₃ and LiTaO₃, it can be effectively removed through selective wet cleaning processes [23, 24]. Unfortunately, an equivalent wet cleaning method for BTO has not yet been found. In the Supplementary §S1, we present experimental examples of how common post-etch wet cleaning methods – including RCA-1, hot piranha, KOH, and buffered oxide etch (BOE) – were either found to cause BTO damage or were ineffective in removing the redeposited materials. Other recent studies have reported redeposition mitigation during etching [18, 19], but this comes with the cost of reduced sidewall verticality, which exacerbates bending loss and compromises optical confinement.

In this work, we report the development of a fabrication process for monolithic BTO-on-insulator photonic integrated circuits, without any undesirable residues, very low surface roughness, and near-optimal sidewall geometry. Using this, we experimentally demonstrate the highest resonator intrinsic quality factor ($Q_i > 1$ million) and lowest propagation loss (0.32 dB/cm) ever measured in any BTO integrated photonics platform.

Our optimized etching process uses Ar⁺ ion milling as the primary physical etch for BTO, and a small fraction of Cl₂ gas is introduced to chemically remove the sputtered material into volatile byproducts which are pumped out of the chamber without forming residue. This process improvement is inspired by an approach that was explored for Ar⁺ etching of lithium niobate [25]. The starting substrate is 340 nm thick a-oriented BTO film on 3 μm thick SiO₂ on a silicon handle wafer (Fig. 1a). A chromium (Cr) hard mask was deposited and patterned using 150 keV electron beam lithography (EBL, Elionix ELS-G150) with ZEP-520A resist. The exposed BTO was then etched to a depth of 180 nm at an etch rate of ≈ 17.5 nm/min using inductively coupled plasma reactive ion etching (ICP-RIE), followed by Cr mask removal.

An ideal waveguide etch profile must exhibit smooth sidewalls and high verticality to ensure optical confinement. To validate the optimized etch process, we present scanning electron microscope (SEM) images of the microring resonator and zoom-in view of waveguide region (Fig. 1b), which show smooth, redeposition-free sidewalls. Further assessment using atomic force microscopy (AFM) and height profile analysis (Fig. 1c,d) reveals a trapezoidal waveguide

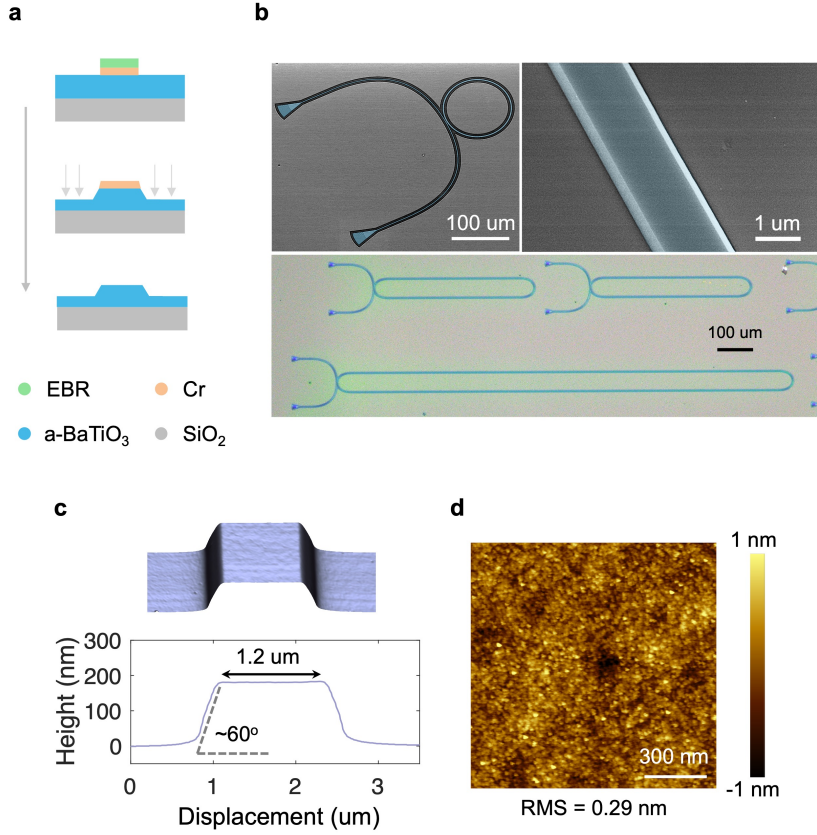


Figure 1: Low loss thin-film barium titanate on insulator integrated photonics. (a) Schematic fabrication flow for monolithic BTO ridge waveguide devices. Electro-beam lithography on ZEP-520A e-beam resist (EBR) is used to define a Cr hardmask, followed by BTO etching via Ar⁺ ion milling (with small fraction of Cl₂ gas), and then Cr removal using a wet etch. (b) Scanning electron microscope (SEM) image of monolithic BTO microring resonator and waveguide. Bottom optical microscope image shows BTO microracetrack resonator. (c) Atomic force microscope (AFM) scan image of our BTO-on-insulator waveguide, with a 1D slice showing a sidewall angle nearly 60°. (d) 2D AFM scan of the etched surface shows etched surface roughness of ≈ 0.29 nm rms.

cross-section with a top width of ≈ 1.2 μm , sidewall angles of $\approx 60^\circ$, and an etch depth of 180 nm. A 2D AFM scan indicates an rms surface roughness of 0.29 nm, confirming excellent surface smoothness conducive to low optical scattering and bending loss.

Fig. 2 presents a comprehensive optical characterization of the fabricated microracetrack and ring resonators, based on measurements taken in the telecom band. First, Fig. 2a shows a representative transmission spectrum through the bus waveguide of a 200 μm -turn radius microracetrack resonator, measured near 1520 nm, displaying the resonance dip of near-critical coupling. For this device we measure intrinsic quality factor $Q_i = 1.35 \times 10^6$ and loaded quality

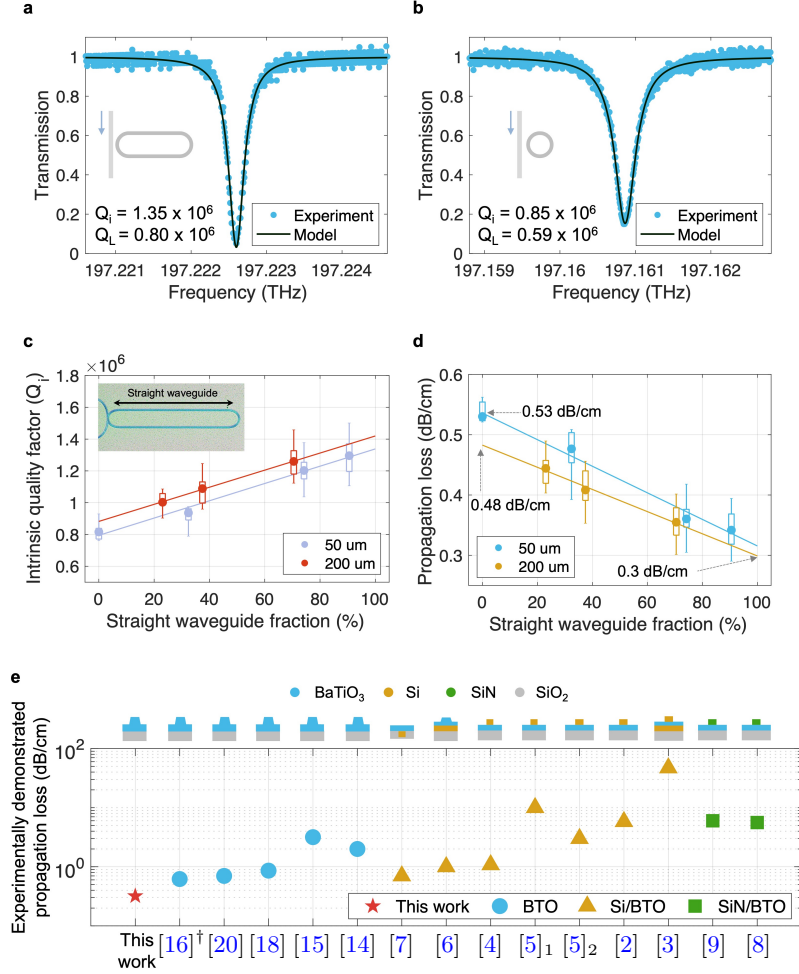


Figure 2: Optical characterization of monolithic BTO-on-insulator microresonators. (a) Resonance line width and quality factor analysis of microracetrack resonator with 200 μm radius with 70.5% straight waveguide fraction, measured near 1520 nm. (b) Quality factor analysis of microring resonator with 50 μm radius. (c) Statistical analysis of measured intrinsic quality factor (Q_i) for resonators with varying straight waveguide fraction, in the range 1520–1537.4 nm (195–197.3 THz). See text for further details. For each set of measurements, the dot shows the mean value, the box represents the interquartile range, and the whiskers denote the minimum and maximum values. (d) Statistical analysis and extrapolation of the propagation loss based on the measurements in (c), leading to an estimated 0.3 dB/cm straight waveguide loss. (e) Benchmarking of the measured propagation loss values from this work and previously reported BTO-based integrated photonics, including monolithic BTO-on-insulator [14–16, 18, 20], Si/BTO hybrid [2–7], and SiN/BTO [8, 9] hybrid. Details are provided in Supplementary Table S1. † Estimated from the data shown in the publication.

factor $Q_L = 0.8 \times 10^6$. To the best of our knowledge, this is the first demonstration of an optical microresonator with Q_i exceeding 1 million, and the highest quality factors (both intrinsic and loaded) in any BTO-based integrated photonics platform. This includes monolithic BTO-on-insulator [16, 18, 19] as well as hybrid structure that incorporate Si [2, 5]. In Fig. 2b we present a representative transmission spectrum (also measured near 1520 nm) for a microring resonator with a tighter bending radius of 50 μm . For this device we estimate quality factors of $Q_i = 0.84 \times 10^6$ and $Q_L = 0.59 \times 10^6$.

In order to determine the linear waveguiding loss, independent of curvature-induced losses, we fabricated a series of microracetrack resonators with varying straight waveguide fraction and two options for turn radius (50 μm and 200 μm). Fig. 2c presents the experimentally extracted intrinsic quality factor Q_i as a function of the straight waveguide fraction. Fig. 2d re-maps this information to an equivalent propagation loss via the relation $\alpha = 2\pi n_g / (Q_i \lambda) \cdot 10 \log_{10} e$ (dB/cm), where n_g is group index and λ is optical wavelength. Measurements for all devices were performed over the range 1520–1537.4 nm (195–197.3 THz), with between 7 to 35 resonances contributing to each data point depending on the device free spectral range. The error bars in Fig. 2c,d represent the statistical variation over all resonances measured for that device.

We find that as the straight waveguide fraction increases, Q_i also increases, confirming that propagation loss is lower in straight sections compared to curved sections. Notably, the 200 μm racetracks consistently exhibit higher Q_i values across all devices, which can be attributed to the larger bend radius and reduced curvature-induced loss. Through linear fit in Fig. 2d we are able to separately extrapolate the loss contributions from straight and curved segments. We therefore estimate the straight waveguide loss to be $\alpha \approx 0.3$ dB/cm, while the bending loss is extracted as ≈ 0.53 dB/cm for the 50 μm bend radius and ≈ 0.48 dB/cm for the 200 μm bend radius. Our best individual result within the statistical data is $\alpha = 0.32$ dB/cm, corresponding to the $Q_i = 1.35 \times 10^6$ individual resonator measurement of Fig. 2a.

To benchmark these results, Fig. 2e presents a comparison of measured propagation losses reported from various BTO photonic platforms, including monolithic BTO-on-insulator [14–16, 18, 20] and hybrid integrations with Si [2–7] and SiN_x [8, 9, 11] (details are provided in Supplementary Table S1). Our best result $\alpha = 0.32$ dB/cm represents the lowest measured propagation loss to date for any BTO-based integrated photonics platform, i.e. without relying on extrapolations. We attribute this improvement to the significantly reduced optical loss enabled by smooth and highly vertical etched sidewalls, which control both scattering and bending losses.

A major motivation for monolithic BTO photonics is the potential for highly efficient electro-optic (EO) modulators and optical switches. To explore this in our platform, we fabricated simple Mach–Zehnder modulators (MZMs) as shown in Fig. 3. We focused our design on optical TE mode waveguides in the a-orientation BTO-on-insulator substrate (i.e., with the [100] axis crystal orientation out-of-plane), with simple electrodes that produce a transverse elec-

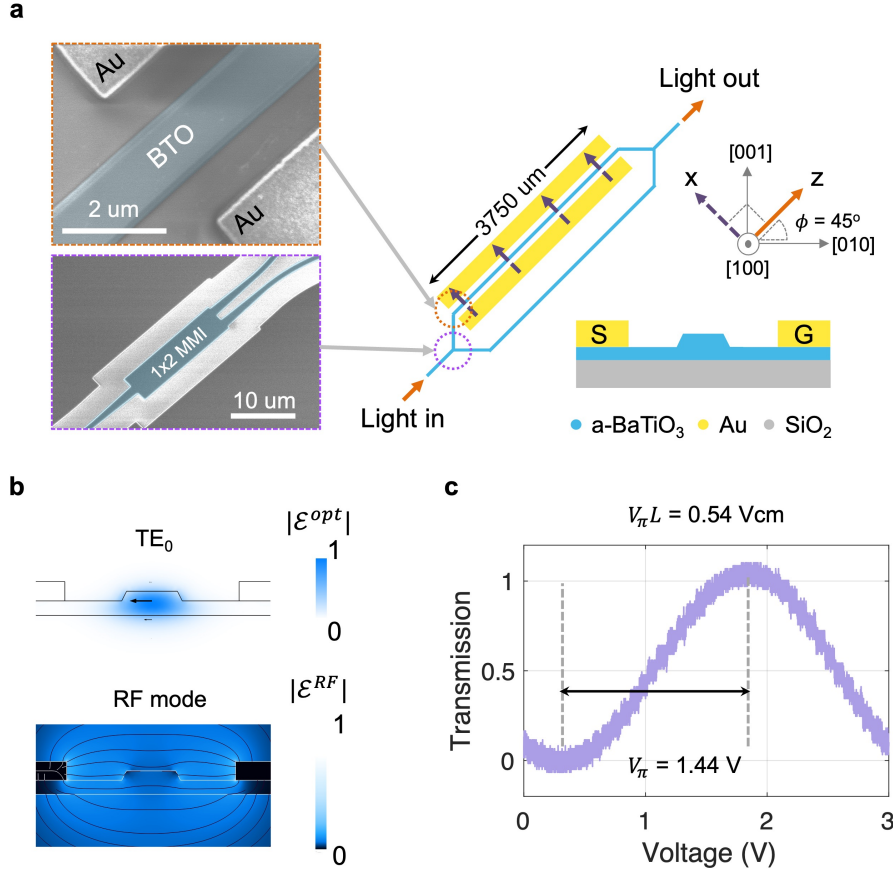


Figure 3: Electro-optic modulation analysis (a) Schematic diagram of the Mach-Zehnder modulator (MZM) that was fabricated in thin-film BTO-on-insulator substrate. (b) Finite element analysis simulation of optical TE₀ mode and RF mode within MZM. (c) Top-view SEM image of MZM. Bottom left shows 1x2 multi mode interferometer (MMI) and bottom right image shows EO modulator with waveguide and Au electrode. (d) Measured optical transmission as a function of voltage, indicating $V_\pi = 1.44$ V and $V_\pi L = 0.54$ V·cm.

tric field as shown in Fig. 3a. Since the Pockels tensor is highly anisotropic, this combination produces an effective coefficient [17] expressed as $r_{\text{eff}}(\phi) = r_{33} \cos^3 \phi + (r_{13} + 2r_{42}) \sin^2 \phi \cos \phi$, where ϕ is the angle chosen between the optical propagation axis and the crystallographic [010] axis, as illustrated in Fig. 3a. The effective r_{eff} is maximized near $\phi \approx 54^\circ$. However, since the BTO ferroelectric domains are typically split into two orthogonal predominant in-plane orientations [26], the best practical effect is obtained at $\phi = 45^\circ$ with lateral RF electric field along the $[0\bar{1}1]$ direction.

We designed the single-arm MZM interferometer (Fig. 3a) with arm length 3.75 mm oriented along the [011] axis of the BTO crystal. The gap between the

stimulus electrodes was set to 3.6 μm . We pole the BTO by applying dc voltage of 120 V across the stimulus electrodes for 30 minutes prior to measurement, corresponding to a maximum E-field of 333 kV/cm (Fig. 3b). In Fig. 3c we present the measured transmission through the MZM as a function of applied voltage across the electrodes, showing the expected sinusoidal dependence due to phase modulation within the interferometer. From this data, we extract a half-wave voltage of $V_\pi = 1.44$ V and $V_\pi \times L = 0.54$ V-cm.

We can now estimate the effective Pockels coefficient through the equation $r_{\text{eff}} = \lambda g / (n^3 \Gamma V_\pi L)$ where $V_\pi L$ is obtained from the MZM experimental measurements, n is refractive index of BTO (≈ 2.26 at 1550 nm), g is the electrode gap, and Γ is the overlap integral between optical mode and electric field [15, 17]. Here we calculate $r_{\text{eff}} \approx 162$ pm/V, which is significantly higher than the largest Pockels tensor element available in lithium niobate, and comparable to past works on monolithic BTO-on-insulator photonics [15, 17, 19]. Since the electro-optic response of BTO is sensitive to the polarization state and domain orientation, which requires proper poling [27]. Therefore, the effective r_{eff} could further improved by implementing enhanced poling techniques, such as with dedicated sidewall electrodes [28]. Such improvements could further unlock the full potential of the Pockels effect in BTO for integrated photonics.

The development of high quality material growth, patterning, and etching processes has been key to the enormous success of integrated photonics platforms using Si, SiN_x , LiNbO_3 , LiTaO_3 , and will similarly be the key to the successful development of monolithic BTO-on-insulator technologies. The progress we have demonstrated is a major enabling step for a wide range of high-performance photonic applications requiring large nonlinear optical coefficients and long photon lifetimes, including frequency combs (electro-optic and Kerr combs) [29, 30], higher harmonic generation [31], narrow-linewidth lasers [32], and squeezed light sources [33]. The programmability advantage of BTO, owing to its characteristic as a soft ferroelectric, can be additionally valuable for optical computing [34, 35] and reconfigurable photonics [36, 37].

References

- [1] Johnston, A. & Weingart, J. Determination of the Low-Frequency Linear Electro-Optic Effect in Tetragonal BaTiO₃. *Journal of the Optical Society of America* **55**, 828–834 (1965).
- [2] Abel, S. *et al.* A Hybrid Barium Titanate–Silicon Photonics Platform for Ultraefficient Electro-Optic Tuning. *Journal of Lightwave Technology* **34**, 1688–1693 (2016).
- [3] Eltes, F. *et al.* Low-Loss BaTiO₃ –Si Waveguides for Nonlinear Integrated Photonics. *ACS Photonics* **3**, 1698–1703 (2016).

- [4] Abel, S. *et al.* Large Pockels effect in micro- and nanostructured barium titanate integrated on silicon. *Nature Materials* **18**, 42–47 (2019).
- [5] Eltes, F. *et al.* A BaTiO₃-Based Electro-Optic Pockels Modulator Monolithically Integrated on an Advanced Silicon Photonics Platform. *Journal of Lightwave Technology* **37**, 1456–1462 (2019).
- [6] Posadas, A. B., Stenger, V. E., DeFouw, J. D., Warner, J. H. & Demkov, A. A. RF-sputtered Z-cut electro-optic barium titanate modulator on silicon photonic platform. *Journal of Applied Physics* **134**, 073101 (2023).
- [7] Tao, M. *et al.* Towards high quality transferred barium titanate ferroelectric hybrid integrated modulator on silicon. *Light: Advanced Manufacturing* **5**, 1 (2024).
- [8] Ortmann, J. E. *et al.* Ultra-Low-Power Tuning in Hybrid Barium Titanate–Silicon Nitride Electro-optic Devices on Silicon. *ACS Photonics* **6**, 2677–2684 (2019).
- [9] Eltes, F. *et al.* An integrated optical modulator operating at cryogenic temperatures. *Nature Materials* **19**, 1164–1168 (2020).
- [10] Posadas, A. B. *et al.* Thick BaTiO₃ Epitaxial Films Integrated on Si by RF Sputtering for Electro-Optic Modulators in Si Photonics. *ACS Applied Materials & Interfaces* **13**, 51230–51244 (2021).
- [11] Kohli, M. *et al.* Plasmonic Ferroelectric Modulator Monolithically Integrated on SiN for 216 GBd Data Transmission. *Journal of Lightwave Technology* **41**, 3825–3831 (2023).
- [12] Reynaud, M. *et al.* Microstructural analysis and electro-optic properties of thick epitaxial BaTiO₃ films integrated on silicon (001). *Physical Review Materials* **6**, 095201 (2022).
- [13] Guo, W., Posadas, A. B. & Demkov, A. A. Epitaxial integration of BaTiO₃ on Si for electro-optic applications. *Journal of Vacuum Science & Technology A: Vacuum, Surfaces, and Films* **39**, 030804 (2021).
- [14] Petraru, A., Schubert, J., Schmid, M. & Buchal, C. Ferroelectric BaTiO₃ thin-film optical waveguide modulators. *Applied Physics Letters* **81**, 1375–1377 (2002).
- [15] Dong, Z. *et al.* Monolithic Barium Titanate Modulators on Silicon-on-Insulator Substrates. *ACS Photonics* **10**, 4367–4376 (2023).
- [16] Raju, A. *et al.* High-Q Monolithic Ring Resonators in Low-Loss Barium Titanate on Silicon. *Laser & Photonics Reviews* 2402086 (2025).
- [17] Chelladurai, D. *et al.* Barium titanate and lithium niobate permittivity and Pockels coefficients from megahertz to sub-terahertz frequencies. *Nature Materials* **24**, 868–875 (2025).

- [18] Riedhauser, A. *et al.* Absorption loss and Kerr nonlinearity in barium titanate waveguides. *APL Photonics* **10**, 016121 (2025).
- [19] Möhl, C. *et al.* Bidirectional microwave-optical conversion with an integrated soft-ferroelectric barium titanate transducer (2025). ArXiv:2501.09728 [physics].
- [20] Isti, M. I. A. *et al.* Fabrication and Optical Characterization of Low-Loss Barium Titanate Waveguides. *IEEE Photonics Technology Letters* **37**, 1101–1104 (2025).
- [21] Li, Y., Wang, C., Yao, Z., Kim, H.-K. & Kim, N.-Y. Comparative analysis of barium titanate thin films dry etching using inductively coupled plasmas by different fluorine-based mixture gas. *Nanoscale Research Letters* **9**, 530 (2014).
- [22] Cheng, J. *et al.* Nanoscale etching of perovskite oxides for field effect transistor applications. *Journal of Vacuum Science & Technology B, Nanotechnology and Microelectronics: Materials, Processing, Measurement, and Phenomena* **38**, 012201 (2020).
- [23] Ulliac, G., Calero, V., Ndao, A., Baida, F. & Bernal, M.-P. Argon plasma inductively coupled plasma reactive ion etching study for smooth sidewall thin film lithium niobate waveguide application. *Optical Materials* **53**, 1–5 (2016).
- [24] Wang, C. *et al.* Lithium tantalate photonic integrated circuits for volume manufacturing. *Nature* **629**, 784–790 (2024).
- [25] Younesi, M. *et al.* Fabrication of low-loss lithium niobate on insulator waveguides on the wafer scale. *Optical Materials Express* **15**, 299 (2025).
- [26] Demkov, A. A. & Posadas, A. B. Ferroelectric BaTiO₃ for Electro-Optic Modulators in Si Photonics. *IEEE Journal of Selected Topics in Quantum Electronics* **30**, 1–13 (2024).
- [27] Posadas, A. B., Wilson, A. B. & Demkov, A. A. Effect of poling voltage on electro-optic response of epitaxial BaTiO₃ on Si grown by sputtering. In *2024 IEEE Silicon Photonics Conference (SiPhotonics)*, 1–2 (IEEE, Tokyo Bay, Japan, 2024).
- [28] Franken, C. A. A. *et al.* Milliwatt-level UV generation using sidewall poled lithium niobate (2025). ArXiv:2503.16785 [physics].
- [29] Zhang, M. *et al.* Broadband electro-optic frequency comb generation in a lithium niobate microring resonator. *Nature* **568**, 373–377 (2019).
- [30] Del’Haye, P. *et al.* Optical frequency comb generation from a monolithic microresonator. *Nature* **450**, 1214–1217 (2007).

- [31] Moore, J., Tomes, M., Carmon, T. & Jarrahi, M. Continuous-wave cascaded-harmonic generation and multi-photon Raman lasing in lithium niobate whispering-gallery resonators. *Applied Physics Letters* **99**, 221111 (2011).
- [32] Jin, W. *et al.* Hertz-linewidth semiconductor lasers using CMOS-ready ultra-high-Q microresonators. *Nature Photonics* **15**, 346–353 (2021).
- [33] Safavi-Naeini, A. H. *et al.* Squeezed light from a silicon micromechanical resonator. *Nature* **500**, 185–189 (2013).
- [34] Ahmed, S. R. *et al.* Universal photonic artificial intelligence acceleration. *Nature* **640**, 368–374 (2025).
- [35] Ou, S. *et al.* Hypermultiplexed integrated photonics-based optical tensor processor. *Science Advances* **11**, 11 (2025).
- [36] Liu, W. *et al.* A fully reconfigurable photonic integrated signal processor. *Nature Photonics* **10**, 190–195 (2016).
- [37] Prabhathan, P. *et al.* Roadmap for phase change materials in photonics and beyond. *iScience* **26**, 107946 (2023).

Acknowledgments

The authors would like to acknowledge invaluable support from Dr. Edmond Chow and Dr. Soo Ho Choi at the Holonyak Micro & Nanotechnology Lab at the University of Illinois at Urbana-Champaign, from Dr. Agham Posadas at La Luce Cristallina, and from Dr. Brian Kasch at the Air Force Research Laboratory (AFRL) Space Vehicles Directorate. This work was sponsored by the AFRL / US Space Force grant FA9453-20-2-0001, the US Office of Naval Research (ONR) Multi-University Research Initiative grant N00014-20-1-2325, and the Defense Advanced Research Projects Agency (DARPA) under Cooperative Agreement D24AC00003. The views and conclusions contained herein are those of the authors and should not be interpreted as necessarily representing the official policies or endorsements, either expressed or implied, of DARPA, AFRL, ONR, or the US Government.

Data availability

The data that support the findings of this study are available from the corresponding authors upon reasonable request.

Author contributions

G.I.K. and G.B. jointly conceived this work. G.I.K. performed the theoretical analysis, performed the device fabrication, and conducted the experiments. G.I.K. and J.Y. analyzed the experimental data. All authors contributed to writing the manuscript. G.B. supervised all aspects of this project.

Supplementary Information:

Low loss monolithic barium titanate on insulator integrated photonics with intrinsic quality factor > 1 million

Gwan In Kim¹, Jieun Yim², and Gaurav Bahl²

¹ Department of Electrical & Computer Engineering,

² Department of Mechanical Science and Engineering,
University of Illinois at Urbana-Champaign, Urbana, IL 61801 USA

S1 Evaluation of wet cleaning strategies for re-deposition removal

On-sidewall redeposition of etch products is a known issue in Ar⁺ ion milling, as it relies on physical ion bombardment. This undesirable redeposition along the etched sidewalls introduces significant roughness and degrades optical propagation loss. While such redeposition is often addressed by post-etch wet cleaning steps in other materials, such as LiNbO₃ and LiTaO₃, there is not yet a comparable method available for BTO.

To make a comparison, we show a BTO etching result using our optimized dry etching process in Fig. S1a on the right. This approach yields smooth BTO sidewalls with no observable etch product redeposition. We can compare this to a more conventional Ar⁺ ion milling process performed on BTO (Fig. S1a on the left), whose the etch recipe is similar to the lithium niobate version [S1, S2], and we observe prominent physical redeposition along the sidewalls.

To evaluate whether various wet cleaning techniques can remove the redeposited material, we tested several commonly used wet cleaning chemistries – including RCA-1, hot piranha, KOH:H₂O₂, and buffered oxide etchant (BOE). As shown in Fig. S1b, RCA-1 cleaning (NH₄OH:H₂O₂:H₂O = 1:1:5, 40 minutes) still leaves substantial redeposition along the sidewalls and introduces surface pinholes. Hot piranha treatment causes pronounced surface etching and morphological damage to the BTO, likely due to its aggressive oxidizing nature. KOH cleaning, which is effective for LiTaO₃ [S3], leads to surface roughening, which is also similarly shown in BOE (6:1) treatment.

These observations collectively suggest that wet cleaning chemistries optimized for other ferroelectric oxides (LiNbO₃ or LiTaO₃) do not translate effectively to BTO. In many cases, they exacerbate surface roughness or induce damage, which is detrimental to low-loss photonic device performance. Therefore, achieving redeposition-free etch profiles in BTO is a welcome strategy.

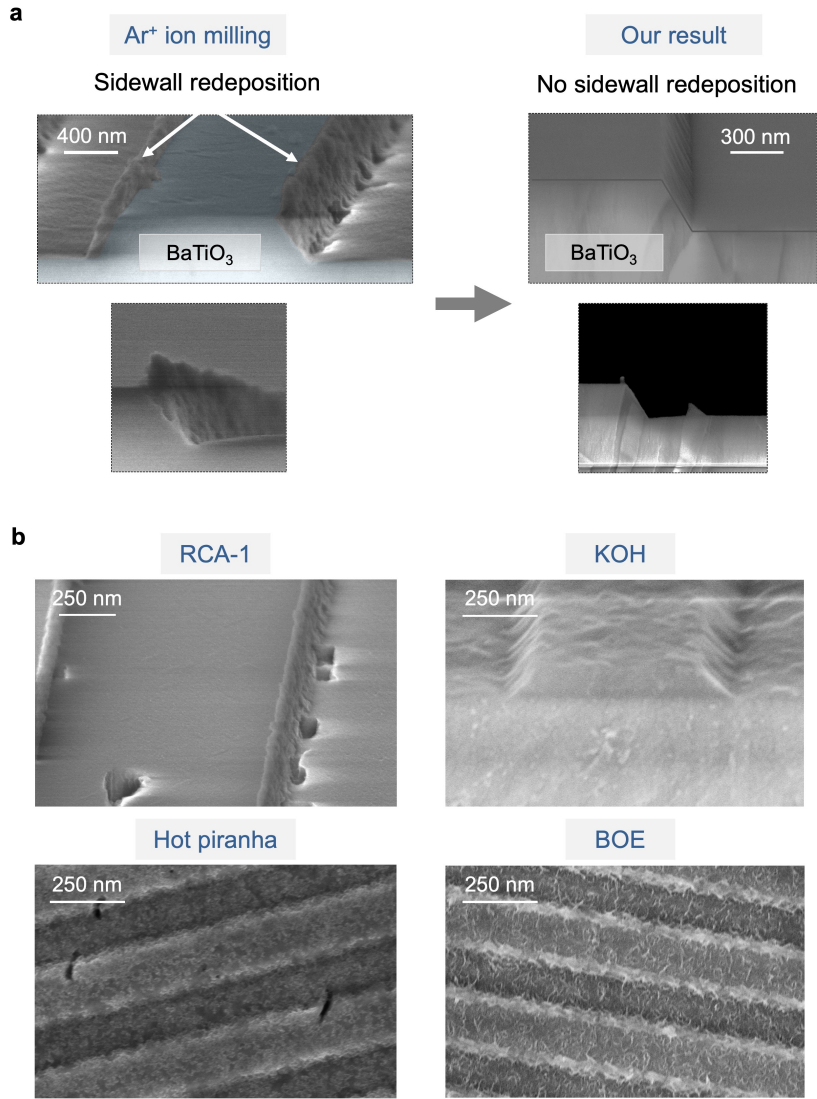


Figure S1: Comparison of sidewall redeposition and wet cleaning effects on BTO waveguides. (a) Cross-sectional SEM images comparing typical Ar⁺ ion milling (left) with our optimized etching process (right). Conventional ion milling results in significant sidewall redeposition, while our process yields smooth, residue-free sidewalls. (b) SEM images showing the effect of various wet cleaning treatments on BTO sidewalls after redeposition. RCA-1 (top left) is not effective and introduces roughness. KOH:H₂O₂ (top right) causes topographical damage. Hot piranha (bottom left) leads to severe surface roughening, and BOE (bottom right) fails to eliminate redeposition and causes additional morphological distortion.

Table S1: Comparison of measured quality factors and propagation losses (i.e. without extrapolation) in various BTO integrated photonics platforms.

Publication	Year	Device Type	Platform	Intrinsic Q-factor (Q_i)	Loaded Q-factor (Q_L)	Propagation loss (α , dB/cm)	Wavelength (nm)
This work		Racetrack Resonator	BTOI	1.35×10^6	0.80×10^6	0.32	1520
		Ring Resonator	BTOI	0.85×10^6	0.59×10^6	0.52	1520
Isti et. al. [S4]	2025	Waveguide	BTOI	N/A	N/A	0.7	1546
Raju et. al. [S5]	2025	Racetrack Resonator	BTOI	0.5×10^6	0.09×10^6	0.62^\dagger	1550
		Ring Resonator	BTOI	0.2×10^6	0.10×10^6	2.11	1550
Riedhauser et. al. [S6]	2025	Resonator	BTOI	0.45×10^6	N/A	0.86	1554
Möhl et. al. [S7]	2025	Resonator	BTOI	0.25×10^6 ($\kappa_i = 776$ MHz at 1550 nm)	N/A	N/A	1537–1577
Dong et. al. [S8]	2023	Waveguide	BTOI	N/A	N/A	3.17	1535–1565
Petraru et. al. [S9]	2002	Waveguide	BTOI	N/A	N/A	2–3	632
Tao et. al. [S10]	2023	Waveguide	Si/BTO	N/A	N/A	1	1545
Posadas et. al. [S11]	2023	Waveguide	Si/BTO	N/A	N/A	1.08	1550
Abel et. al. [S12]	2019	Waveguide	Si/BTO	N/A	N/A	10	1541
Eltes et. al. [S13]	2019	Waveguide Resonator	Si/BTO	N/A	N/A	3	1550–1551
			Si/BTO	N/A	0.05×10^6	5.8	
Abel et. al. [S14]	2016	Resonator	Si/BTO	N/A	0.0046×10^6	47	1555–1575
Eltes et. al. [S15]	2016	Waveguide	Si/BTO	N/A	N/A	6	1550
Kohli et. al. [S16]	2023	Waveguide (plasmonic)	SiN/BTO	N/A	N/A	5000	1557
Eltes et. al. [S17]	2020	Waveguide	SiN/BTO	N/A	N/A	5.6	1511–1512
Ortmann et. al. [S18]	2019	Resonator	SiN/BTO	N/A	N/A	9.4	1550

BTOI = Thin-film barium titanate (BTO)-on-insulator. Si/BTO = Silicon and barium titanate hybrid. SiN/BTO = Silicon nitride and barium titanate hybrid. N/A = Information not available or not applicable.

\dagger Estimated from the data shown in the publication.

Supplementary References

- [S1] Örsel, O. E. & Bahl, G. Electro-optic non-reciprocal polarization rotation in lithium niobate. *APL Photonics* **8**, 096107 (2023).
- [S2] Sohn, D. B., Örsel, O. E. & Bahl, G. Electrically driven optical isolation through phonon-mediated photonic Autler–Townes splitting. *Nature Photonics* **15**, 822–827 (2021).
- [S3] Wang, C. *et al.* Lithium tantalate photonic integrated circuits for volume manufacturing. *Nature* **629**, 784–790 (2024).
- [S4] Isti, M. I. A. *et al.* Fabrication and Optical Characterization of Low-Loss Barium Titanate Waveguides. *IEEE Photonics Technology Letters* **37**, 1101–1104 (2025).
- [S5] Raju, A. *et al.* High-Q Monolithic Ring Resonators in Low-Loss Barium Titanate on Silicon. *Laser & Photonics Reviews* 2402086 (2025).
- [S6] Riedhauser, A. *et al.* Absorption loss and Kerr nonlinearity in barium titanate waveguides. *APL Photonics* **10**, 016121 (2025).
- [S7] Möhl, C. *et al.* Bidirectional microwave-optical conversion with an integrated soft-ferroelectric barium titanate transducer (2025). ArXiv:2501.09728 [physics].
- [S8] Dong, Z. *et al.* Monolithic Barium Titanate Modulators on Silicon-on-Insulator Substrates. *ACS Photonics* **10**, 4367–4376 (2023).
- [S9] Petraru, A., Schubert, J., Schmid, M. & Buchal, C. Ferroelectric BaTiO₃ thin-film optical waveguide modulators. *Applied Physics Letters* **81**, 1375–1377 (2002).
- [S10] Tao, M. *et al.* Towards high quality transferred barium titanate ferroelectric hybrid integrated modulator on silicon. *Light: Advanced Manufacturing* **5**, 1 (2024).
- [S11] Posadas, A. B., Stenger, V. E., DeFouw, J. D., Warner, J. H. & Demkov, A. A. RF-sputtered Z-cut electro-optic barium titanate modulator on silicon photonic platform. *Journal of Applied Physics* **134**, 073101 (2023).
- [S12] Abel, S. *et al.* Large Pockels effect in micro- and nanostructured barium titanate integrated on silicon. *Nature Materials* **18**, 42–47 (2019).
- [S13] Eltes, F. *et al.* A BaTiO₃-Based Electro-Optic Pockels Modulator Monolithically Integrated on an Advanced Silicon Photonics Platform. *Journal of Lightwave Technology* **37**, 1456–1462 (2019).
- [S14] Abel, S. *et al.* A Hybrid Barium Titanate–Silicon Photonics Platform for Ultraefficient Electro-Optic Tuning. *Journal of Lightwave Technology* **34**, 1688–1693 (2016).

- [S15] Eltes, F. *et al.* Low-Loss BaTiO₃-Si Waveguides for Nonlinear Integrated Photonics. *ACS Photonics* **3**, 1698–1703 (2016).
- [S16] Kohli, M. *et al.* Plasmonic Ferroelectric Modulator Monolithically Integrated on SiN for 216 GBd Data Transmission. *Journal of Lightwave Technology* **41**, 3825–3831 (2023).
- [S17] Eltes, F. *et al.* An integrated optical modulator operating at cryogenic temperatures. *Nature Materials* **19**, 1164–1168 (2020).
- [S18] Ortmann, J. E. *et al.* Ultra-Low-Power Tuning in Hybrid Barium Titanate–Silicon Nitride Electro-optic Devices on Silicon. *ACS Photonics* **6**, 2677–2684 (2019).